

**DEVELOPMENT OF NOVEL Mg-Ca-Sc ALLOYS AS  
POTENTIAL BIODEGRADABLE IMPLANT  
MATERIAL**

**CHETAN SINGH**



**DEPARTMENT OF MATERIALS SCIENCE AND  
ENGINEERING  
INDIAN INSTITUTE OF TECHNOLOGY DELHI  
OCTOBER 2022**



© Indian Institute of Technology Delhi (IITD), New Delhi, 2022



**DEVELOPMENT OF NOVEL Mg-Ca-Sc ALLOYS AS  
POTENTIAL BIODEGRADABLE IMPLANT  
MATERIAL**

*by*

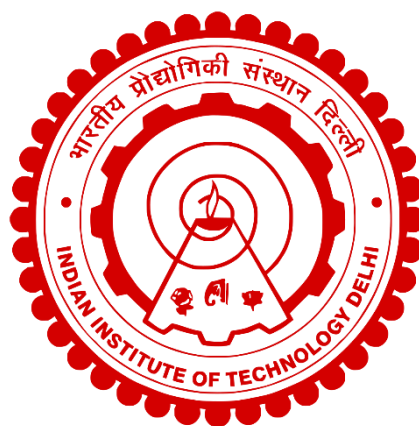
**CHETAN SINGH**

**Department of Materials Science and Engineering**

*Submitted*

**in fulfilment of the requirements of the degree of Doctor of Philosophy**

*to the*



**INDIAN INSTITUTE OF TECHNOLOGY DELHI**

**OCTOBER 2022**



## **CERTIFICATE**

This is to certify that the thesis entitled “**DEVELOPMENT OF NOVEL Mg-Ca-Sc ALLOYS AS POTENTIAL BIODEGRADABLE IMPLANT MATERIAL**” is being submitted by **Mr. CHETAN SINGH** to the Indian Institute of Technology Delhi for the award of the degree of **DOCTOR OF PHILOSOPHY**. This is a record of bonafide research work carried out by him under our supervision and guidance. The matter presented in this thesis has not been submitted, in part or in full to any other University or Institute for the award of any degree or diploma.

**Prof. Jayant Jain**

Associate Professor

Department of Materials Science and Engineering

Indian Institute of Technology Delhi

## **Acknowledgements**

Writing this thesis has been a challenging but rewarding process. Many people helped and guided me to finish this thesis. This thesis allowed me to work directly with a brilliant supervisor. So, first and foremost, I would like to express my profound and sincere gratitude to my supervisor, Prof. Jayant Jain, for his encouragement and excellent guidance during my tenure here as a Research Scholar. This thesis would not have been possible without his timely and untiring guidance. He has been incredibly supportive and has given me the freedom to carry out my work in the manner I wished to execute. His vast pool of ideas, excellent time management skills, and tremendous enthusiasm for research and teaching have been a constant inspiration for me. The knowledge and experience gained from the research work, teaching assistantship, and various projects assigned to me will guide me through my future endeavours.

I would also like to thank SRC members Prof. Rajesh Prasad, Prof. Suresh Neelakantan and Prof. Deepak Kumar for providing me with invaluable suggestions and serving on my committee during the tenure. I would also like to thank Prof. Sudhanshu Shekhar Singh for helping me with various experiments like stress corrosion cracking and discussions at different stages of my work. I want to thank the Department of Materials Science and Engineering for allowing me to use various instruments and taking care of my official needs. Special mention to Mr. Mohit, Mr. Brijesh, and Mr. S. B. Prasad for allowing me to access and learn various scientific pieces of equipment here at IIT Delhi. Thanks to the management of the Karakoram hostel for making my stay comfortable. Needless to say, the hostel will always be missed.

Life is better with friends. A big thanks to a friend, mentor, big brother, and senior, Dr. Aditya Gokhale, for teaching the experimental facilities and providing guidance and

support. I would like to thank Dr. Deepak Chauhan for being there as a senior, teaching me the nitty-gritty of FE-SEM, specimen preparation, and giving thoughtful suggestions. Thanks to my beloved colleagues – Dr. Vickey Nandal, Dr. Prashant Mittal, Dr. Nooruddin Ansari, Shrikanth S, Ranjeet Kumar, Amit Prasad, Kasimuthumaniyan S, Priyanka Saini, Ashwani Kumar, Ayushi Thakur, Shivansh Mehrotra, Rashi R, Karthik Kumar, Ashitha Pattabi, Syed Junaid and Subhakar for making the workspace a lively place to work and learn. I am fortunate and thankful to have friends like Abhishek Rastogi, Himanshu Rai, Bushra Harun, Ayushi Neema, Swati Sharma, Abhinay Pardeshi, Vivek Chaudhary, Mukund Shastri and Paras Kasotiya. They are always ready to lend an ear during my ups and downs. I would like to express my appreciation to Aaliya for accepting my impractical sentimentality; your encouragement and belief in me enabled me to live a reality that otherwise would have remained a dream.

Finally, this thesis is dedicated to the memory of my father, Mr. Sunil Kumar, who had always supported me and helped me become who I am today. My mother, Mrs. Anita Rani, never stopped to amaze me with her love, support, and fortitude. She encourages me to nurture academic as well as cultural aspects, as she is the perfect example of an all-round personality. My brother, Mr. Aman Kumar, for his unwavering support and confidence and for being my pillar of strength. He is extremely protective and loving and has never let me down all these years. I will always be grateful for their upbringing and the countless sacrifices, support, and trust they gave me to become the person I am today.

**CHETAN SINGH**

## **Abstract**

Magnesium (Mg) based alloys have attracted significant attention as potential biodegradable implant materials owing to their good biocompatibility, superior osteogenesis ability and admissible biodegradability. However, their higher corrosion rate limits widespread applicability, which degrades the mechanical integrity of the magnesium implant even before the damaged tissue has healed. Therefore, it is necessary to design and develop an Mg-based alloy with improved corrosion resistance having acceptable mechanical and tribological properties. The drawbacks mentioned above can be overcome by effective alloying and thermomechanical processing. However, the alloying addition in the case of biomaterials should be chosen such that the byproducts of the alloy degradation should not be toxic so that the biocompatibility of Mg is not compromised. Among alloying elements, rare-earth (RE) elements enhance corrosion resistance by preferentially forming an impermeable protective layer, grain refinement and removing impurity elements via the scavenger effect. Scandium (Sc) is the most promising RE alloying addition as it unprecedentedly enhances the biocompatibility and corrosion resistance of the Mg alloy.

However, the high cost of RE elements limits their addition in significant quantity. Thus, to develop a cost-effective implant material, the addition of calcium (Ca) as an alternate alloying element to Mg alloys has been considered as Ca provides all the specified biomedical benefits. However, the concentration of Ca was restricted at 0.6 wt. % to avoid a higher volume fraction of detrimental intermetallic  $Mg_2Ca$  phase. Therefore, Sc as a ternary addition to the binary Mg-0.6Ca alloy was explored. First, a pseudo-binary Mg-0.6Ca-xSc phase diagram was developed using ThermoCalc, which exhibited enhanced solubility on simultaneous addition. Then Mg-0.6Ca-xSc alloys were developed through a die casting process. In the current dissertation, the influence

of Sc as a ternary addition on the deformation, corrosion, mechanical, and wear behaviour is investigated to evaluate the potential of the developed novel alloy compositions.

The produced alloys were thermomechanically processed to achieve desired microstructural features, for instance, finer grain size and strong basal texture. During thermomechanical processing, the effect of simultaneous addition of non-rare-earth (Ca) and rare-earth (Sc) elements on the hot-rolled deformation behaviour, recrystallization and texture evolution of Mg alloys is evaluated. The simultaneous addition of Ca and Sc resulted in the desired microstructural features. Based on the results of thermomechanical processing, the Sc concentration was restricted to 0.5 wt. % as the gains on further Sc addition was not cost-effective.

The influence of Sc as a ternary addition and thermomechanical processing on the corrosion behaviour of Mg-0.6Ca binary alloy was explored. The Sc addition resulted in improved corrosion resistance. *In-situ* corrosion study was performed on an as-cast Mg-0.6Ca binary alloy to develop an understanding of the activated corrosion mechanism. Additionally, the cytotoxicity of the developed novel composition was studied, where the developed Mg-0.6Ca-xSc alloys exhibited negligible cytotoxicity.

Further, the influence of Sc addition on the mechanical viz tensile and compression behaviour was studied. The Sc addition up to 0.5 wt. % did not significantly affect the mechanical properties, as compared to other RE additions. *In-situ* tensile study was performed on recrystallized Mg-0.6Ca binary alloy to develop an understanding of the deformation and fracture behaviour. The tensile testing was done at multiple strain rates to explore the strain rate sensitivity as Ca addition is known to increase the strain rate sensitivity.

The stress corrosion cracking (SCC) and wear behaviour of the developed novel alloys were studied in 0.9 wt. % NaCl to study the influence of the combined effect of corrosive media and mechanical strain. The SCC behaviour was studied using the slow strain rate testing method under tensile strain. The wear experimentation utilised a ball-on-disc tribometer with the countersurface as an alumina ball. The analysis of the wear track was performed using field emission scanning electron microscopy (FESEM) and a 3D profilometer to understand the underlying wear mechanisms and calculate the wear rate. The Sc containing alloys exhibited reduced susceptibility to SCC and improved wear resistance.

In summary, the present study reports a systematic study starting from the development of Mg-0.6Ca-xSc alloys to exploring the mechanical, electrochemical, tribological and cytotoxic behaviour to develop a comprehensive understanding of the developed alloy compositions.

## सार

मैग्नीशियम (Mg) आधारित मिश्र धातुओं ने अपनी अच्छी जैव-अनुकूलता, बेहतर अस्थिजनन क्षमता और स्वीकार्य जैव-अवक्रमण क्षमता के कारण संभावित जैव-अवक्रमणीय प्रत्यारोपण सामग्री के रूप में महत्वपूर्ण ध्यान आकर्षित किया है। हालांकि, उनकी उच्च संक्षारण दर व्यापक प्रयोज्यता को सीमित करती है, जो क्षतिग्रस्त ऊतक के ठीक होने से पहले ही मैग्नीशियम प्रत्यारोपण की यांत्रिक अखंडता को कम कर देती है। इसलिए, स्वीकार्य यांत्रिक और ट्राइबोलॉजी गुणों वाले बेहतर संक्षारण प्रतिरोध के साथ मैग्नीशियम-आधारित मिश्र धातु को डिजाइन और विकसित करना आवश्यक है। ऊपर वर्णित कमियों को प्रभावी मिश्र धातु और थर्मोमेकेनिकल प्रसंस्करण द्वारा दूर किया जा सकता है। हालांकि, बायोमैटिरियल्स के मामले में मिश्र धातु को इस तरह से चुना जाना चाहिए कि मिश्र धातु के बायोप्रोडक्ट्स जहरीले न हों ताकि मैग्नीशियम की बायोकम्पैटिबिलिटी से समझौता न हो। मिश्र धातु तत्वों में, दुर्लभ-पृथ्वी तत्व अधिमानतः एक अभेद्य सुरक्षात्मक परत बनाकर, ग्रेन शोधन और मेहतर प्रभाव के माध्यम से अशुद्धता तत्वों को हटाकर संक्षारण प्रतिरोध को बढ़ाते हैं। स्कैंडियम (Sc) सबसे आशाजनक दुर्लभ-पृथ्वी मिश्रधातु है क्योंकि यह अभूतपूर्व रूप से मैग्नीशियम मिश्र धातु की जैव-अनुकूलता और संक्षारण प्रतिरोध को बढ़ाता है।

हालांकि, दुर्लभ-पृथ्वी तत्वों की उच्च लागत महत्वपूर्ण मात्रा में उनके अतिरिक्त योग को सीमित करती है। इस प्रकार, एक लागत प्रभावी प्रत्यारोपण सामग्री विकसित करने के लिए, कैल्शियम (Ca) को वैकल्पिक मिश्र धातु तत्व के रूप में मैग्नीशियम मिश्र धातु के रूप में जोड़ने पर विचार किया गया है क्योंकि कैल्शियम सभी निर्दिष्ट जैव चिकित्सा लाभ प्रदान करता है। हालांकि, कैल्शियम की सांद्रता 0.6 प्रतिशत वजन पर प्रतिबंधित है हानिकारक इंटरमेटेलिक  $Mg_2Ca$  के उच्च मात्रा अंश से बचने के लिए। इसलिए, बाइनरी  $Mg-0.6Ca$  मिश्र धातु के लिए एक टर्नरी जोड़ के रूप में स्कैंडियम का

उपयोग किया गया। सबसे पहले, थर्मोकैल्क का उपयोग करके एक छद्म-बाइनरी  $Mg-0.6Ca-xSc$  चरण आरेख विकसित किया गया था, जो एक साथ जोड़ पर बढ़ी हुई घुलनशीलता का प्रदर्शन करता था। फिर  $Mg-0.6Ca-xSc$  मिश्र धातुओं को डार्क फ्लाइ प्रक्रिया के माध्यम से विकसित किया गया। वर्तमान शोध प्रबंध में, विकसित उपन्यास मिश्र धातु रचनाओं की क्षमता का मूल्यांकन करने के लिए विरूपण, जंग, यांत्रिक और घिसाव के व्यवहार पर एक त्रिगुट जोड़ के रूप में स्कैंडियम के प्रभाव की जांच की गई है।

उत्पादित मिश्र धातुओं को वांछित सूक्ष्म संरचनात्मक विशेषताओं को प्राप्त करने के लिए थर्मोमेकेनिकल रूप से संसाधित किया गया था, उदाहरण के लिए, महीन ग्रेन का आकार और मजबूत बेसल बनावट। थर्मोमेकेनिकल प्रोसेसिंग के दौरान, गैर-दुर्लभ-पृथ्वी (कैल्शियम) और दुर्लभ-पृथ्वी (स्कैंडियम) तत्वों के साथ-साथ हॉट-रोल्ड विरूपण व्यवहार, मैग्नीशियम मिश्र धातुओं के पुनः क्रिस्टलीकरण और बनावट विकास पर प्रभाव का मूल्यांकन किया जाता है। कैल्शियम और स्कैंडियम के एक साथ जोड़ के परिणामस्वरूप वांछित सूक्ष्म संरचनात्मक विशेषताएं हुईं। थर्मोमेकेनिकल प्रोसेसिंग के परिणामों के आधार पर, स्कैंडियम एकाग्रता 0.5 प्रतिशत वजन तक सीमित थी क्योंकि प्रतिशत वजन योग के रूप में आगे स्कैंडियम जोड़ पर लाभ लागत प्रभावी नहीं था।

$Mg-0.6Ca$  बाइनरी मिश्र धातु के जंग व्यवहार पर टर्नरी जोड़ और थर्मोमेकेनिकल प्रसंस्करण के रूप में स्कैंडियम के प्रभाव का पता लगाया गया था। स्कैंडियम जोड़ के परिणामस्वरूप संक्षारण प्रतिरोध में सुधार हुआ। सक्रिय जंग तंत्र की समझ विकसित करने के लिए इन-सीटू जंग अध्ययन एक कास्ट  $Mg-0.6Ca$  बाइनरी मिश्र धातु पर किया गया था। इसके अतिरिक्त, विकसित उपन्यास रचना की साइटोटोक्सिसिटी का अध्ययन किया गया, जहां विकसित  $Mg-0.6Ca-xSc$  मिश्र धातुओं ने नगण्य साइटोटोक्सिसिटी का प्रदर्शन किया।

इसके अलावा, यांत्रिक जैसे तन्यता और संपीडन व्यवहार पर स्कैंडियम जोड़ के प्रभाव का अध्ययन किया गया था। अतिरिक्त 0.५ तक अन्य दुर्लभ-पृथ्वी तत्वों परिवर्धन की तुलना में स्कैंडियम ने यांत्रिक गुणों को महत्वपूर्ण रूप से प्रभावित नहीं किया। विरूपण और फ्रैक्चर व्यवहार की समझ विकसित करने के लिए पुनः क्रिस्टलीकृत Mg-0.६Ca बाइनरी मिश्र धातु पर इन-सीटू तन्यता अध्ययन किया गया था। तनाव दर संवेदनशीलता का पता लगाने के लिए तन्यता परीक्षण कई तनाव दरों पर किया गया था क्योंकि कैल्शियम अतिरिक्त तनाव दर संवेदनशीलता को बढ़ाने के लिए जाना जाता है।

तनाव जंग क्रैकिंग और विकसित उपन्यास मिश्र धातुओं के घिसाव के व्यवहार का 0.९ प्रतिशत सोडियम क्लोराइड घोल में अध्ययन किया गया था, संक्षारक मीडिया और यांत्रिक तनाव के संयुक्त प्रभाव के प्रभाव का अध्ययन करने के लिए। तनाव जंग क्रैकिंग व्यवहार का अध्ययन तन्यता तनाव के तहत धीमी गति दर परीक्षण पद्धति का उपयोग करके किया गया था। घिसाव के प्रयोग में एल्यूमिना बॉल के रूप में काउंटर-सतह के साथ एक बॉल-ऑन-डिस्क ट्राइबोमीटर का उपयोग किया। घिसाव के ट्रैक का विश्लेषण क्षेत्र उत्सर्जन स्कैनिंग इलेक्ट्रॉन माइक्रोस्कोपी और एक ३डी प्रोफिलोमीटर का उपयोग करके अंतर्निहित घिसाव के तंत्र को समझने और घिसाव की दर की गणना करने के लिए किया गया था। स्कैंडियम युक्त मिश्र धातुओं ने तनाव जंग क्रैकिंग के प्रति कम संवेदनशीलता और बेहतर घिसाव के प्रतिरोध का प्रदर्शन किया।

संक्षेप में, वर्तमान अध्ययन एक व्यवस्थित अध्ययन की रिपोर्ट करता है जो Mg-0.६Ca-xSc मिश्र धातुओं के विकास से शुरू होकर विकसित मिश्र धातु रचनाओं की व्यापक समझ विकसित करने के लिए यांत्रिक, विद्युत रासायनिक, ट्राइबोलॉजी और साइटोटोक्सिक व्यवहार की खोज करता है।

# Table of Contents

CERTIFICATE.....	i
Acknowledgements.....	ii
Abstract.....	iv
Table of Contents.....	x
List of Figures.....	xvi
List of Tables.....	xxviii
Chapter 1 Introduction.....	1
Chapter 2 Literature Review.....	6
2.1 Introduction.....	6
2.2 Evolution of metallic implants materials.....	6
2.3 Degradation behaviour of biodegradable metals.....	10
2.3.1 Corrosion.....	10
2.3.1.1 Thermodynamics of corrosion.....	11
2.3.1.2 Kinetics of Corrosion.....	12
2.3.2 Wear.....	14
2.3.2.1 Adhesive wear.....	15
2.3.2.2 Abrasive wear.....	17
2.3.2.3 Oxidation wear.....	18
2.4 Magnesium as a biodegradable metal.....	19
2.5 Deformation and annealing behaviour of Mg and its alloys.....	22

2.5.1	Slip modes in Mg .....	22
2.5.2	Twin modes in Mg .....	24
2.5.3	Grain boundary sliding in Mg alloys .....	26
2.5.4	Hot deformation in Mg alloys.....	27
2.5.5	Recrystallization in Mg alloys .....	29
2.5.5.1	Grain boundary nucleation .....	31
2.5.5.2	Subgrain boundary migration .....	33
2.5.5.3	Shear band nucleation (SBN) .....	35
2.5.5.4	Deformation twinning nucleation.....	36
2.5.5.5	Particles stimulated nucleation (PSN) .....	38
2.5.6	Influence of alloying elements on texture.....	39
2.6	Corrosion behaviour of Mg and its alloys.....	44
2.6.1	Factors influencing the corrosion behaviour.....	45
2.6.1.1	Influence of the grain size .....	46
2.6.1.2	Influence of the second phase.....	46
2.6.1.3	Influence of the alloying elements.....	48
2.6.2	Stress corrosion cracking behaviour .....	53
2.6.3	Summary .....	57
2.7	Wear under corrosive and non-corrosive media of Mg and its alloys .....	57
2.7.1	Factors influencing wear behaviour.....	59
2.7.1.1	Influence of the microstructure.....	59
2.7.1.2	Influence of the orientation.....	60
2.7.1.3	Influence of the alloying elements.....	62

2.7.2	Summary .....	63
2.8	Alloy development strategy of a novel Mg alloy .....	64
2.8.1	Impurity control .....	64
2.8.2	Alloying element selection .....	64
2.8.3	Alloy families.....	65
2.8.3.1	Mg-Al based alloys.....	67
2.8.3.2	Mg-Zn based alloys .....	67
2.8.3.3	Mg-Si based alloys .....	68
2.8.3.4	Mg-Zr based alloys .....	68
2.8.3.5	Mg-RE based alloys.....	69
2.8.3.6	Mg-Ca based alloys .....	72
2.8.4	Cytotoxicity.....	75
2.9	Overall summary .....	77
Chapter 3	Motivation and Objectives .....	79
Chapter 4	Materials and Methodology .....	82
4.1	Introduction .....	82
4.2	Initial material .....	82
4.3	Alloy development .....	82
4.4	Thermomechanical processing.....	84
4.5	Metallography preparation procedure .....	87
4.6	Material characterization techniques.....	88
4.6.1	Optical Microscopy.....	88

4.6.2	Scanning Electron Microscopy (SEM) .....	88
4.6.3	Electron backscattered diffraction (EBSD) analysis.....	90
4.6.4	Texture measurement .....	92
4.6.5	Raman spectroscopy .....	93
4.6.6	Atomic force spectroscopy .....	94
4.7	Mechanical testing.....	94
4.7.1	Tensile test .....	94
4.7.2	Compression test.....	97
4.7.3	Wear test .....	99
4.8	Corrosion test .....	102
4.8.1	Immersion test.....	102
4.8.2	Potential stabilization.....	104
4.8.3	Electrochemical potentiodynamic polarization measurements.....	105
4.8.4	Electrochemical impedance spectroscopy .....	106
4.8.5	Cell culture.....	108
4.9	Stress corrosion cracking .....	108
Chapter 5 Mg-Ca-Sc alloys: high-temperature deformation mechanism, texture and recrystallization behaviour.....		110
5.1	Introduction .....	110
5.2	Alloy development and initial microstructure.....	111
5.3	Hot rolling deformation behaviour and dynamic recrystallization .....	114
5.4	As-rolled and annealed macro-texture .....	121
5.4.1	Annealed microstructure .....	125
5.5	Summary .....	127

Chapter 6	Mg-Ca-Sc alloys: corrosion and cytotoxicity behaviour .....	129
6.1	Introduction .....	129
6.2	Immersion test .....	130
6.3	Potentiodynamic polarization measurements .....	132
6.4	Electrochemical impedance spectroscopy (EIS) measurements .....	134
6.5	Characterization of the corrosion products .....	137
6.6	Corrosion mechanism.....	140
6.6.1	Role of Mg <sub>2</sub> Ca phase .....	140
6.6.2	Role of grain size and texture .....	145
6.7	Cytotoxicity.....	147
6.8	Summary .....	149
Chapter 7	Mg-Ca-Sc alloys: mechanical and tribological behaviour.....	151
7.1	Introduction .....	151
7.2	Initial microstructure .....	152
7.3	Compression behaviour: Mg-0.6Ca-xSc alloys .....	153
7.4	Tensile behaviour: Mg-0.6Ca-xSc alloys.....	156
7.5	<i>In-situ</i> tensile behaviour: Mg-0.6Ca alloy.....	159
7.6	Stress corrosion cracking behaviour: Mg-0.6Ca-xSc alloys .....	166
7.7	Tribological behaviour: Mg-0.6Ca-xSc alloys.....	169
7.7.1	Friction behaviour.....	169
7.7.2	Wear behaviour.....	171
7.7.3	Characterization of the worn surface .....	173

7.8	Summary .....	178
Chapter 8	Conclusions and Future work .....	181
8.1	Conclusions .....	181
8.2	Future work .....	184
References	.....	185

## List of Figures

Figure 1.1: Comparison of density and mechanical properties of metallic implant materials with natural bone highlighting that magnesium exhibits least deviation [4, 10, 27].	3
Figure 2.1: Schematic diagram of (a) tribological system and (b) interdependencies and properties of tribological system [52].	15
Figure 2.2: Schematic diagram of adhesive wear [53].	16
Figure 2.3: SEM micrograph of adhesive wear in AM60 [54].	16
Figure 2.4: Schematic diagram showing two-body abrasion [53].	17
Figure 2.5: Schematic diagram showing three-body abrasion [53].	17
Figure 2.6: SEM micrograph of the abrasive wear of AM50B [55].	18
Figure 2.7: Schematic diagram showing oxidative wear [53].	19
Figure 2.8: SEM micrograph of the oxidative wear of AM60B [54].	19
Figure 2.9: Schematic diagrams of various slip systems in HCP Mg (a) basal slip, (b) prismatic slip, (c) pyramidal slip $a$ , (d) 1 <sup>st</sup> order pyramidal $c + a$ and (e) 2 <sup>nd</sup> order pyramidal $c + a$ .	23
Figure 2.10: Schematic diagrams showing the re-orientation of the $c$ axis resulting from (a) 1012 extension and (b) 1011 contraction twinning in Mg.	25
Figure 2.11: Microstructure of AZ31 alloy deformed under (a) compression exhibiting lenticular shaped thick 1012 extension twins, and (b) tension exhibiting thin 1011 contraction twin [94].	26
Figure 2.12: Offset formation at the grain boundaries attributed to GBS [103].	27
Figure 2.13: Schematic drawing illustrating the mechanism of CDRX and DDRX [119].	31
Figure 2.14: Nucleation mechanism proposed for recrystallization in Mg alloys.	31

Figure 2.15: Schematic of nucleation at grain boundaries during DRX [121].	32
Figure 2.16: (a) Serrations of grain boundaries during DRX of AZ31 alloy and (b) fine DRX grains at higher magnification [120].	33
Figure 2.17: Schematic illustration of recrystallization by subgrain boundary rotation nucleation mechanism [125].	34
Figure 2.18: EBSD IPF maps of extruded Mg–9.80Gd–3.78Y–1.12Sm–0.48Zr alloy illustrating (a) deformed grain with DRX (b) subgrains (with LAGBS) and DRX grains via subgrain boundary rotation nucleation mechanism [123].	34
Figure 2.19: EBSD maps showing shear band nucleation in cold-rolled Mg-0.3Zn-0.1Ca alloy composition annealed at 623 K at different times [130].	35
Figure 2.20: IPF map of as-deformed Mg-1Gd alloy illustrating dynamic recrystallization in compression and double twins [135]. CD denotes the compression direction.	37
Figure 2.21: Quasi-in situ EBSD maps illustrate twin induced recrystallization in WE43 alloy [134].	37
Figure 2.22: (a) Schematic of the particle deformation zones adjacent to second phase particle, (b) band contrast image of ZWEK1000 Mg-RE alloy and (c) nucleation of grains near the second phase particles [136].	39
Figure 2.23: EBSD maps and respective inverse pole figures of deformed and recrystallized grain in Mg-Gd alloy extruded at 415 °C [141].	40
Figure 2.24: (a) Pole figure intensity in rolled condition and (b) after annealing [142].	42
Figure 2.25: 0002 and 0110 pole figures illustrated (a) the effect of the RE elements on the texture during hot rolling and (b) annealed at 400°C for 1 h [143].	43
Figure 2.26: (1010) and (0002) pole figures illustrating the effect of calcium addition on the annealed texture [145].	44

Figure 2.27: SEM image of as-cast (a) AZ91, (b) AZ91-0.3 wt.%Y and (a1-b1) corrosion morphologies in 5% NaCl after 48 hours [155].	47
Figure 2.28: Optical image of AZ31B with increase in grain size (a-c) and its corrosion morphologies (a1-c1) in 3.5% NaCl after 30 min. [165].	47
Figure 2.29: Schematic illustrating the influence of cathodic $Mg_{17}Al_{12}$ and anodic $Mg_2Ca$ nature of precipitates and their distribution on the corrosion behaviour. ....	51
Figure 2.30: (a) Corrosion current density evaluated from electrochemical tests and (b) corrosion rates after immersion tests of binary Mg-RE alloys and pure Mg [22]. ....	52
Figure 2.31: Optical micrographs of as-cast (a) Mg-1Ca, (b) Mg-2Ca, and (c) Mg-3Ca exhibiting the formation of $Mg_2Ca$ phase at grain boundaries on increasing Ca content [177].	53
Figure 2.32: Fractography of as-cast pure Mg tested under corrosive electrolyte, (a) complete view, (b) high magnification images of a highlighted region in (a) exhibiting fluted and smooth facets, (c) high magnification images of a highlighted region in (b) showing smooth brittle facets, and (d) high magnification images of a highlighted region in (c) showing fluted facets [186].	55
Figure 2.33: SEM micrographs of AZ91-Ca alloy tested in m-SBF (a) macro-view, (b) brittle cracks visible at the edge and (c) cleavage facets and micro-voids visible at higher magnification [190].	56
Figure 2.34: The fractured surface of Mg-Zn-Zr alloy tested in 3.5 wt. % NaCl solution with bimodal grain size distribution with surface area fraction of coarse grains ( $> 20 \mu m$ ) as (a) 2 %, (b) 25 % (c) 48 %, and (d) 95 % [191].	56
Figure 2.35: The variation of coefficient of friction with time for an Mg-Zn-Ca alloy under a dry and corrosive media environment [193].	58

Figure 2.36: SEM images of the wear track under (a) dry conditions and (b) SBF electrolyte lubrication. ....	58
Figure 2.37: Wear rate of as-cast and aged (cast + T6) Mg-11Y-5Gd-2Zn alloys using a ball-on-plate configuration [199]. ....	60
Figure 2.38: Wear volume as a function of orientation and temperature [206]. ....	61
Figure 2.39: SEM images of the scratched region for (a) basal, (b) pyramidal and (c) prismatic orientations at RT [206]. ....	61
Figure 2.40: The variation of weight loss due to wear for Mg-Zn-Ca alloys with different Zn concentrations [193]. ....	63
Figure 2.41: The different criteria for selecting alloying elements for developing Mg-based alloys [18]. ....	66
Figure 2.42 Degradation rates for Mg-X alloys in the as-cast condition function of alloy concentration [216]. ....	66
Figure 2.43: The original screw and segmented screw at 1, 4, and 18 months post-operation [231]. ....	70
Figure 2.44: Optical micrographs of as-cast and etched Mg-3Gd, Mg-3Y and Mg-3Sc alloys [232]. ....	71
Figure 2.45: Isothermal TGA plots of Mg-3Gd, Mg-3Y and Mg-3Sc alloys oxidized at 500 °C [232]. ....	71
Figure 2.46: Phase diagram of the Mg-Sc binary system [234]. ....	72
Figure 2.47: Mg-Ca binary phase diagram [242]. ....	74
Figure 2.48: Compressive and bending yield strength as a function of alloy composition [175]. ....	74

Figure 2.49: The polarization resistance of Mg-Ca alloys as a function of alloy composition [175].	75
Figure 4.1: (a) SwamEquip bottom pouring vacuum die casting furnace, (b) as-cast plates of (b1) Mg-0.6Ca, (b2) Mg-0.6Ca-0.1Sc, and (b3) Mg-0.6Ca-0.5Sc.	84
Figure 4.2: Mg-rich region of (a) binary phase diagram of Mg-Ca (inset shows the zoomed single-phase region) and (b) pseudo-binary phase diagram of Mg-0.6Ca-xSc [249].	86
Figure 4.3: Laboratory two-high rolling mill (Banbros, BRM-15, India).	86
Figure 4.4: Schematic illustration of the thermomechanical processing.	87
Figure 4.5: LectroPol-5, Struers electropolishing machine, (a) control unit, and (b) polishing unit.	89
Figure 4.6: Field emission scanning electron microscope machine (JSM 7800F, JEOL) integrated with energy-dispersive X-ray spectrometer and electron backscattered diffraction detector (Oxford Instruments).	90
Figure 4.7: (a) XRD machine, Rigaku Ultima IV, and (b) magnified view of XRD chamber showing X-ray source, sample holder and detector.	92
Figure 4.8: Micro-Raman spectrometer (Renishaw, UK).	93
Figure 4.9: (a) Universal testing machine integrated with a video extensometer (Zwick/Roell, Germany), and (b) schematic diagram of the tensile specimen.	96
Figure 4.10: (a) Micro tensile testing module of a 10 kN load cell (Kammrath-Weiss), (b) schematic diagram of the <i>in-situ</i> tensile specimen.	97
Figure 4.11: Schematic diagram of the compression sample with a loading direction parallel to the rolling direction.	99

Figure 4.12: (a) Ball-on-disc/plate configuration tribometer testing machine (MFT-5000), (a1, a2) schematics showing geometric configuration, (a3, a4) 2D profilometer images of wear surface for the rotating and reciprocating wear tests, respectively. .... 101

Figure 4.13: Schematic of the experimental setup utilized for wear testing in corrosive media lubricated condition..... 101

Figure 4.14: Mg-0.6Ca-0.5Sc alloy's representative open circuit potential (OCP) against time curve measured just before potentiodynamic polarisation. .... 105

Figure 4.15: (a) Vertical servo-electric slow strain system (BISS-ITW Electra 50), (b) magnified view of the acrylic chamber utilized to hold electrolyte during testing..... 109

Figure 5.1: (a-d) SEM micrographs illustrating the as-cast microstructures, (a1, a2) and b(1-3), c(1-3), and d(1-3) EDS element mapping images showing elemental distribution for Mg-0.6Ca, Mg-0.6Ca-0.1Sc, Mg-0.6Ca-0.5Sc and Mg-0.6Ca-1.0Sc, respectively. .... 113

Figure 5.2: XRD patterns of as-cast Mg-0.6Ca, Mg-0.6Ca-0.1Sc, Mg-0.6Ca-0.5Sc, and Mg-0.6Ca-1.0Sc. All the observed peaks belong to Mg..... 114

Figure 5.3: (a-d) Band contrast maps superimposed with grain boundary, (a1-d1) LAM maps of hot rolled 50% at 723 K Mg-0.6Ca, Mg-0.6Ca-0.1Sc, Mg-0.6Ca-0.5Sc, and Mg-0.6Ca-1.0Sc, respectively. .... 116

Figure 5.4: (a-e) Grain boundary misorientation profile, along with IPF of preferred misorientation axis for special boundaries at 5–10°, 30–40°, 50–60°, and 85–90° of 50% hot-rolled at 723 K of Mg-0.6Ca, Mg-1.0Sc, Mg-0.6Ca-0.1Sc, Mg-0.6Ca-0.5Sc, and Mg-0.6Ca-1.0Sc, respectively. .... 118

Figure 5.5: {1 0 1 1} contraction twin boundary and {1 0 1 2} extension twin boundary fraction as a function of alloy composition..... 119

Figure 5.6: (a, b) Grain reference orientation deviation (GROD) map superimposed with grain boundaries and sub-grain boundaries, (a1, b1) EBSD IPF maps, the inset is pole figure of dynamic recrystallized grains and (a2, b2) EBSD IPF maps, the inset is pole figure of parent grains corresponding to (a, b) of 50% hot-rolled at 723 K of Mg-0.6Ca and Mg-1.0Sc, respectively. .... 120

Figure 5.7: (a, b, c) Grain reference orientation deviation (GROD) map superimposed with grain boundaries and sub-grain boundaries (a1, b1, c1) EBSD IPF maps, the inset is pole figure of dynamic recrystallized grains, (a2, b2, c2) EBSD IPF maps, the inset is pole figure of parent grains corresponding to (a, b, c) of 50% hot-rolled at 723 K of Mg-0.6Ca-0.1Sc, Mg-0.6Ca-0.5Sc, and Mg-0.6Ca-1.0Sc, respectively. .... 122

Figure 5.8: Basal {0002} pole figures showing the texture of (a-e) 50% hot-rolled at 723 K and (a1-e1) recrystallized Mg-0.6Ca, Mg-1.0Sc, Mg-0.6Ca-0.1Sc, Mg-0.6Ca-0.5Sc, and Mg-0.6Ca-1.0Sc, respectively..... 124

Figure 5.9: Maximum basal intensity as a function of alloy composition for as-rolled and annealed samples. .... 124

Figure 5.10: EBSD IPF maps after annealing for 5 min at 623 K of (a) Mg-0.6Ca, (b) Mg-1.0Sc, (c) Mg-0.6Ca-0.1Sc, (d) Mg-0.6Ca-0.5Sc, and (e) Mg-0.6Ca-1.0Sc. .... 126

Figure 5.11: Grain size distribution after annealing for 5 min at 623 K of Mg-0.6Ca, Mg-1.0Sc, Mg-0.6Ca-0.1Sc, Mg-0.6Ca-0.5Sc, and Mg-0.6Ca-1.0Sc..... 126

Figure 6.1: Corrosion rates of the as-cast and recrystallized Mg-0.6Ca-xSc alloys after immersion in 0.9 wt. % NaCl solution for 15 days..... 131

Figure 6.2: Corrosion rate of the developed novel Mg-0.6Ca-0.5Sc alloy in recrystallized condition compared to conventional Mg-alloys [284, 285]..... 131

Figure 6.3: Open circuit potential of Mg–0.6Ca-xSc recrystallized alloys measured during 1 h of exposure in 0.9 wt. % sodium chloride solution.....	133
Figure 6.4: Potentiodynamic polarization curves for Mg-0.6Ca-xSc recrystallized alloys. ....	133
Figure 6.5: Corrosion rate (mm/year) for Mg-0.6Ca-xSc alloys as determined from the PDP curves.....	134
Figure 6.6: Experimental Nyquist plots for the Mg-0.6Ca-xSc alloys. ....	136
Figure 6.7: The equivalent circuit diagram used for fitting EIS data. ....	136
Figure 6.8: (a-c) SEM micrographs and ((a-c)(1-3) corresponding EDS elemental maps of recrystallized Mg-0.6Ca, Mg-0.6Ca-0.1Sc, and Mg-0.6Ca-0.5Sc alloys, respectively, after immersion test for 15 days illustrating the surface post corrosion along with the distribution of magnesium (Mg), oxygen (O), calcium/scandium (Ca/Sc) for recrystallized Mg-0.6Ca-xSc alloys.....	139
Figure 6.9: Magnified SEM images of the recrystallized (a) Mg-0.6Ca, (b) Mg-0.6Ca-0.1Sc, and (c) Mg-0.6Ca-0.5Sc after immersion in 0.9 wt. % NaCl for 15 days. ....	139
Figure 6.10: Raman spectra from the corrosion products formed after electrochemical tests in 0.9 wt.% NaCl solution on the recrystallized Mg-0.6Ca, Mg-0.6Ca-0.1Sc and Mg-0.6Ca-0.5Sc alloys. ....	140
Figure 6.11: (a, b) SEM images and (a1, b1) EDS line analysis of the eutectic micro-constituent before and after corrosion, respectively. ....	143
Figure 6.12: The <i>in-situ</i> surface appearance of as-cast Mg-0.6Ca immersed in 0.9 wt. % NaCl solution after (a) 80 s, (b) 110 s, (c) 120 s, and (d) 450 s exhibiting hydrogen evolution. ....	143

Figure 6.13: The *in-situ* surface appearance of as-cast Mg-0.6Ca immersed in 0.9 wt. % NaCl solution after (a) 80 s, and (b) 300 s, (a1) and (b1) the schematic representation of the corrosion process. .... 144

Figure 6.14: Side view schematic representation of the corrosion process demonstrating the (a) remote cathodic site and (b) generation of hydrogen stream on the corrosion front. .... 145

Figure 6.15: Average grain size and maximum basal texture intensity as a function of alloy composition for recrystallized condition. .... 146

Figure 6.16: Live-dead assay exhibiting MG63 cells after 48 h seeding in the presence of Mg extracts stained with (a-d) calcein-AM showing live cells (green) and (a1-d1) stained with propidium iodide (red) showing dead cells..... 148

Figure 6.17: The cell viability using the indirect method in the presence of Mg-0.6Ca-xSc and AZ31 [310] alloys in pre-conditioned extract for 48 h. The quantitative data are reported as a percentage of the number of viable cells in Mg-0.6Ca-xSc extract compared to the number of viable cells in an unmodified cell culture medium (Control)..... 148

Figure 7.1: EBSD IPF maps showing the microstructure of as-cast (a) Mg-0.6Ca, (b) Mg-0.6Ca-0.1Sc, and (c) Mg-0.6Ca-0.5Sc..... 152

Figure 7.2: EBSD IPF mas showing the microstructure of recrystallized (a) Mg-0.6Ca, (b) Mg-0.6Ca-0.1Sc, and (c) Mg-0.6Ca-0.5Sc..... 153

Figure 7.3: (a, b) Compressive engineering stress-strain curves showing the mechanical properties of Mg-0.6Ca-xSc alloys in as-cast and recrystallized conditions, respectively. .... 154

Figure 7.4: SEM micrographs of the fractured surfaces of as-cast (a) Mg-0.6Ca, (b) Mg-0.6Ca-0.1Sc, and (c) Mg-0.6Ca-0.5Sc..... 155

Figure 7.5: (a, b) Tensile engineering stress-strain curves showing the mechanical properties of Mg-0.6Ca-xSc alloys in as-cast and recrystallized conditions, respectively. .... 157

Figure 7.6: Tension compression yield asymmetry as a function of alloy composition for as-cast and recrystallized conditions..... 158

Figure 7.7: Tensile engineering stress-strain curves at multiple strain rates ( $10^{-3} - 10^{-5}$ )  $s^{-1}$  of recrystallized Mg-0.6Ca alloy. .... 161

Figure 7.8: Double logarithmic plot showing strain rate dependence of stress with the black line showing the linear fitting used to calculate strain rate sensitivity. .... 161

Figure 7.9: (a, b, c) SEM micrographs and (a1, b1, c1) reconstructed 3D surface topography images obtained (a, a1) before and after *in-situ* tensile tests carried out at (b, b1)  $10^{-4} s^{-1}$  and (c, c1)  $10^{-5} s^{-1}$  strain rates, respectively. The corresponding line profiles along the highlighted red lines in the SEM micrographs are shown in (a2, b2, c2)..... 162

Figure 7.10: SEM micrographs of the alloy deformed at  $10^{-5} s^{-1}$  strain rate at 30 % strain exhibiting cavitation..... 163

Figure 7.11: Activation energy for plastic deformation as a function of different Mg-alloys [98, 325, 328, 329]. .... 164

Figure 7.12: SEM micrographs (a) before loading, (b-d) sequence of in-situ SEM micrographs showing the crack propagation at 10 %, 28 %, and 45% strain, respectively. The in-situ tensile tests were carried out at a  $10^{-5} s^{-1}$  strain rate. .... 165

Figure 7.13: Fractography of the recrystallized Mg-0.6Ca alloy tested under tension at a strain rate of  $10^{-5} s^{-1}$ . (Note: The yellow arrowheads highlight the tear ridge formation, and the black arrowheads highlight the cleavage facets)..... 166

Figure 7.14: Engineering stress-strain curves of Mg<sub>0.6</sub>Ca-xSc alloys obtained from SSRT at a strain rate of  $10^{-7}$  in 0.9 wt. % NaCl solution..... 168

Figure 7.15: SEM micrographs of the fractured surfaces of the as-cast (a) Mg-0.6Ca, (b) Mg-0.6Ca-0.1Sc, (c) Mg-0.6Ca-0.5Sc alloys tested in 0.9 wt. % NaCl electrolyte at a strain rate of  $10^{-7} \text{ s}^{-1}$ . Note (a1, b1, c1) are the magnified images of selected areas in (a, b, c), respectively. (Note: The white arrowheads highlight the blister-like features, whereas the yellow arrowhead highlights the intergranular fracture) ..... 168

Figure 7.16: Average coefficient of friction as a function of alloy composition under dry and 0.9 wt. % NaCl electrolyte lubricated conditions. .... 170

Figure 7.17: (a, b, c) SEM micrographs of the near edge area of the wear scars of Mg-0.6Ca, Mg-0.6Ca-0.1Sc, and Mg-0.6Ca-0.5Sc, respectively, under dry sliding condition..... 170

Figure 7.18: Wear rate of Mg-0.6Ca-xSc alloys under dry sliding and 0.9 wt. % NaCl lubrication condition. .... 172

Figure 7.19: : (a-c) SEM micrographs of the wear scar and corresponding EDS elemental mapping showing the distribution of Mg, oxygen (O), calcium (Ca) and scandium (Sc) for recrystallized Mg-0.6Ca, Mg-0.6Ca-0.1Sc, and Mg-0.6Ca-0.5Sc alloys, respectively under dry sliding condition. (Note: yellow arrowheads highlight the ridges and groove, and the yellow circle highlight delamination). .... 174

Figure 7.20: (a-c) SEM micrographs of the wear scar and corresponding EDS elemental mapping showing the distribution of Mg, oxygen (O), calcium (Ca) and scandium (Sc) for recrystallized Mg-0.6Ca, Mg-0.6Ca-0.1Sc, and Mg-0.6Ca-0.5Sc alloys, respectively under 0.9 wt. % NaCl solution lubrication condition. .... 177

Figure 7.21: (a, b, c) Magnified SEM micrographs of the highlighted regions of the wear scars in Figure 7.20(a, b, c) of Mg-0.6Ca, Mg-0.6Ca-0.1Sc, and Mg-0.6Ca-0.5Sc,

respectively under lubricated condition. (Note: The yellow arrowhead highlights the ridge formation, and the elliptical region highlights delamination).....178

## List of Tables

Table 2.1: Metallic materials advantages, disadvantages, and applications [11, 16] .....	8
Table 2.2: Mechanical properties of natural bone and magnesium [10, 49, 71].....	21
Table 2.3: Slip systems and associated CRSS values in Mg single crystal .....	23
Table 4.1: Chemical composition (wt.%) of Mg-0.6Ca-xSc alloys.....	83
Table 6.1: Electrolyte and charge transfer resistance, electrical double layer capacitance, film resistance and constant phase capacitance values determined from Nyquist plots fitting .....	137
Table 7.1: Compressive mechanical properties of Mg-0.6Ca-xSc alloys in the as-cast and recrystallized condition.....	155
Table 7.2: Tensile mechanical properties of Mg-0.6Ca-xSc alloys in the as-cast and recrystallized condition.....	157